Journal of Nuclear Materials 600 (2024) 155265

Contents lists available at ScienceDirect

Journal of Nuclear Materials

journal homepage: www.elsevier.com/locate/jnucmat

Microstructural analysis of ex-service neutron irradiated stainless steel nuclear fuel cladding by high-speed AFM

S. Moore [a,*], R. Burrows [b], A.D. Warren [a], D. Hambley [c], F.S. Russell-Pavier [a], T.L. Martin [a], L. Picco [d,e], O.D. Payton [a,e]

[a] Interface Analysis Centre, HH Wills Physics Laboratory, University of Bristol, Bristol, UK, BS8 1TL
[b] National Nuclear Laboratory, Building 102B, Stonehouse Park, Sperry Way, Stonehouse, Gloucestershire, UK, GL10 3UT
[c] National Nuclear Laboratory, Central Laboratory, Sellafield, Seascale, Cumbria CA20 1PG, UK
[d] Department of Physics, Virginia Commonwealth University, VA, United States
[e] Bristol Nano Dynamics Ltd., Bristol, United Kingdom

HIGHLIGHTS

- Novel analysis of ex-service fuel cladding by high-speed AFM and electron microscopy.
- $M_{23}C_6$, sigma phase, NbC, and G phase precipitates identified in cladding material.
- High-speed AFM analysis of precipitates revealed surface textures unique to each type.
- Numerous nanometre-scale voids were observed across the surface by high-speed AFM.
- An association was found between void frequency and grain boundary type.

ARTICLE INFO

Keywords:
Irradiation
Austenitic stainless steel
AGR fuel cladding
High-speed atomic force microscopy
Characterisation
Correlative microscopy
Electron backscatter diffraction

ABSTRACT

Fuel cladding in advanced gas-cooled nuclear reactors is made of an austenitic stainless steel referred to as 20Cr/25NiNb. This material can undergo microstructural changes in these extreme environments through a combination of thermal effects and radiation damage. In this work, the microstructures present in an ex-service irradiated 20Cr/25Ni-Nb sample are studied using correlated high-speed atomic force microscopy (HS-AFM) and electron microscopy techniques for the first time. Correlated topographic, crystallographic, and chemical information from the sample surface enabled identification of secondary phase precipitates (SPPs) including $M_{23}C_6$, sigma phase, NbC, and G phase. These SPPs can have adverse effects on the material properties. HS-AFM analysis showed surface textures unique to each SPP. Voids formed due to irradiation were also identified across the surface by HS-AFM. These voids were found to be larger in size and depth along grain boundaries. Further analysis identified a relationship between void size and frequency and grain boundary misorientation and SPP presence.

1. Introduction

Fuel cladding in advanced gas-cooled reactors (AGRs) is composed of 20Cr/25Ni-Nb as it is capable of withstanding the extreme conditions of the reactor environment [1–4]. This material also acts as the primary containment for fuel during post-reactor storage, prior to the identification of disposal routes, such as at a geological disposal facility [2–6].

Neutron irradiation in combination with high temperatures is known to alter stainless steel microstructure through neutron damage and thermal effects [1,7]. Historically, extensive research has been performed on the microstructure and physical and corrosion properties of this clad material. However, AGR reactor conditions have changed considerably since these studies, operating at higher burn-up as a result of longer dwell times. There is a need for additional research to highlight any differences in chemical composition and the microstructures observed as a result of the current operating conditions. This is particularly important when identifying safe disposal routes and avoiding localised corrosion processes such as stress corrosion cracking (SCC).

* Corresponding author.
E-mail address: stacy.moore@bristol.ac.uk (S. Moore).

https://doi.org/10.1016/j.jnucmat.2024.155265
Received 19 March 2024; Received in revised form 30 May 2024; Accepted 26 June 2024
Available online 4 July 2024

20Cr/25Ni-Nb is a niobium-stabilised austenitic stainless steel, with 20 wt.% chromium and 25 wt.% nickel, a typical composition is given in Table 1 [7]. Niobium is added to 20Cr/25Ni-Nb as it is a strong carbide former and, following a prior stabilisation heat treatment, results in the formation of niobium carbide (NbC) precipitates within the matrix [1]. The formation of NbC removes carbon from the metal matrix, impeding the formation of chromium-rich carbides that can result in chromium depletion at grain boundaries and susceptibility to localised corrosion [1]. Despite this, chromium depletion along grain boundaries can still occur as a result of prolonged exposure to high temperatures and neutron fluxes [1,7,8].

Neutron irradiation during in-reactor service can induce changes in a materials microstructure including radiation induced sensitisation (RIS) [9–14], void/helium bubble formation [10,11], and the enhancement/induction of secondary phase precipitate (SPP) formation [10,15,16]. Non-irradiated 20Cr/25Ni-Nb is known to contain NbC precipitates, with other precipitates (such as sulphides and oxides) appearing less frequently [6,17]. Upon ageing and irradiation, SPPs commonly identified include: $M_{23}C_6$ precipitates (where M is principally chromium), sigma phase (FeCr), and G phase ($Ni_{16}Nb_6Si_7$) [17,18]. These microstructural changes can be detrimental to the chemical and mechanical properties of the steel which may impact corrosion behaviour during post-service storage. It is therefore important to perform detailed analysis of ex-service specimens, and to identify techniques which enable high throughput evaluation.

High-speed atomic force microscopy (HS-AFM) is capable of producing high-resolution topographic maps of microstructures present on the surface of a sample [19,20]. The contact mode HS-AFM used within this work was developed at the University of Bristol and Bristol Nano Dynamics Ltd. (UK). The high throughput of this technique allowed for large area maps to be collected with nanometre lateral resolution and subatomic height resolution. Data collected over large areas may then be stitched to form a composite map of the region or used to build up statistics about specific features across the surface, such as size and distribution [21–24].

In this work, a series of measurements are performed using HS-AFM on ex-service AGR cladding samples in order to evaluate the microstructural changes caused by irradiation and heating. Additional measurements are performed by complementary techniques, including scanning electron microscopy (SEM) methods, such as electron backscatter diffraction (EBSD) to attain crystallographic information and energy-dispersive X-ray spectroscopy (EDX) to map the elemental composition. By correlating these techniques, this study also explores the capabilities of HS-AFM to establish whether topographic measurements may be used to evaluate SPP identification.

2. Materials and methods

2.1. Ex-service AGR fuel cladding

AGR fuel stringer assemblies contain 8 fuel elements, each containing 36 fuel pins, with the first fuel element located at the bottom of the stringer [25]. The sample of ex-service AGR fuel cladding (20Cr/25Ni-Nb, approximate composition given in Table 1) analysed in this study was collected from a fuel pin in the sixth element of a stringer. Over the course of operation, this element operated at a burnup of 34.5 GWd/tU and a temperature of approximately 735 °C. The estimated dose of the analysed material is 7.2 dpa. Samples collected from this fuel pin have been analysed previously by the UK's National Nuclear Laboratory (NNL).

Table 1
Elemental composition of AGR fuel cladding, given in weight %, from [7].

C	Si	Mn	P	S	Cr	Nb	Ni	Fe
0.062	0.58	0.79	0.014	0.019	19.33	0.56	24.05	Bal.

The sample for analysis was produced by cutting out a 1 mm diameter disc from a pin section using a punch. This disc was ground down from both sides to a thickness of approximately 100 μm and mounted in a gold washer before electropolishing in a solution of 5 % perchloric acid in methanol at −50 °C to produce a smooth surface for HS-AFM and SEM analysis.

2.2. High-speed atomic force microscopy (HS-AFM)

The contact-mode HS-AFM used within this work was a *Vector* Dynamic Scanning Probe Microscope (D-SPM) from Bristol Nano Dynamics Ltd., UK. This instrument builds up topographic maps of a sample by measuring the response of a probe at the end of a cantilever as it is scanned across the surface. The HS-AFM uses Sharp Microlever (MSNL) probes manufactured by Bruker from silicon nitride, with a silicon tip. These probes are a type of contact-mode cantilever with a tip radius of 2–12 nm, a tip height of 2–8 μm, and a spring constant of 0.01 N m^{-1}. Within the set-up used in this work, cantilever displacement is measured using an interferometric detection system which measures the z-displacement of the cantilever to within ±15pm.

Appropriate safety precautions were implemented during handling and imaging of the irradiated stainless steel. A shield made of perspex and lead layers was used in this work to protect the operator during imaging and the HS-AFM was operated at a distance of approximately 4 m.

Topographic data was analysed post-collection using Gwyddion SPM data processing software [26] to produce topographic maps. Bespoke software was used for creating the large composite HS-AFM images [27]. Statistical analysis of the data was performed using Nanomapping software from Bristol Nano Dynamics Ltd. (UK).

2.3. Scanning electron microscopy (SEM) techniques

SEM analysis was performed using a Zeiss ΣIGMA™ Variable Pressure (VP) Field Emission SEM (Oberkochen, Germany. Serial: 03–72) equipped with a Gemini™ electron source. EBSD instrumentation from EDAX-AMETEK Inc. (Mahwah, NJ, USA) included a Digiview™ high-speed digital camera.

EDX maps were collected at a constant beam voltage of 30 kV, an aperture of 120 μm, and a 200 ms dwell time, and analysed using EDAX TEAM software. EBSD analysis was carried out using a beam voltage of 30 kV, an aperture of 120 μm, and a step size of 50 nm using OIM™ data collection and analysis software. The data points were mapped in a hexagonal grid pattern at 120 points per second (double-clock), using the software's 8 × 8 pixel binning setting. Following collection, raw data was cleaned up by filtering points with a confidence index less than 0.1 and using confidence index standardisation.

3. Results

3.1. Large area surface analysis

The sample surface was first observed optically, as shown in Fig. 1a. A number of large SPPs are observed across the surface as dark spots. Fig. 1b shows a secondary electron (SE) image of the surface in which numerous SPPs and grains are observed, these SPPs are primarily observed to be intergranular.

Topographic measurements by HS-AFM were collected from the region outlined in red (approximately 60 μm × 60 μm) in Fig. 1a. Individual frames were stitched together to form composite images, shown in Fig. 2a. Large SPPs are highlighted as white features distributed across the image. These features have a high aspect ratio and result in the immediate surrounding areas to exhibit image artefacts due to flattening post-processing. A number of grain boundaries are also observed within the region, some appearing darker than the bulk indicating that they have been preferentially etched during sample preparation. Slip bands

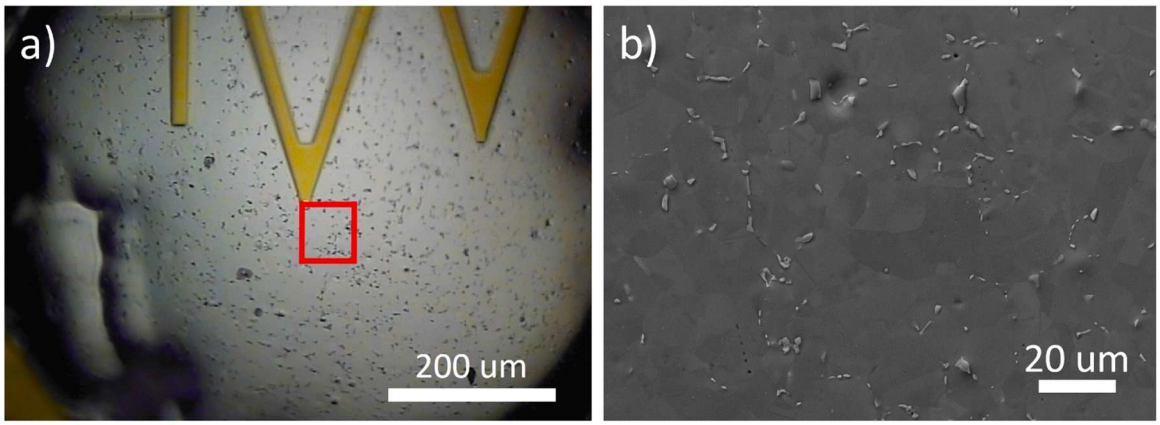

Fig. 1. Images showing the sample surface: a) an optical image with the region of analysis outlined in red, b) an SE image collected at 30 kV from a region containing the area outlined in red.

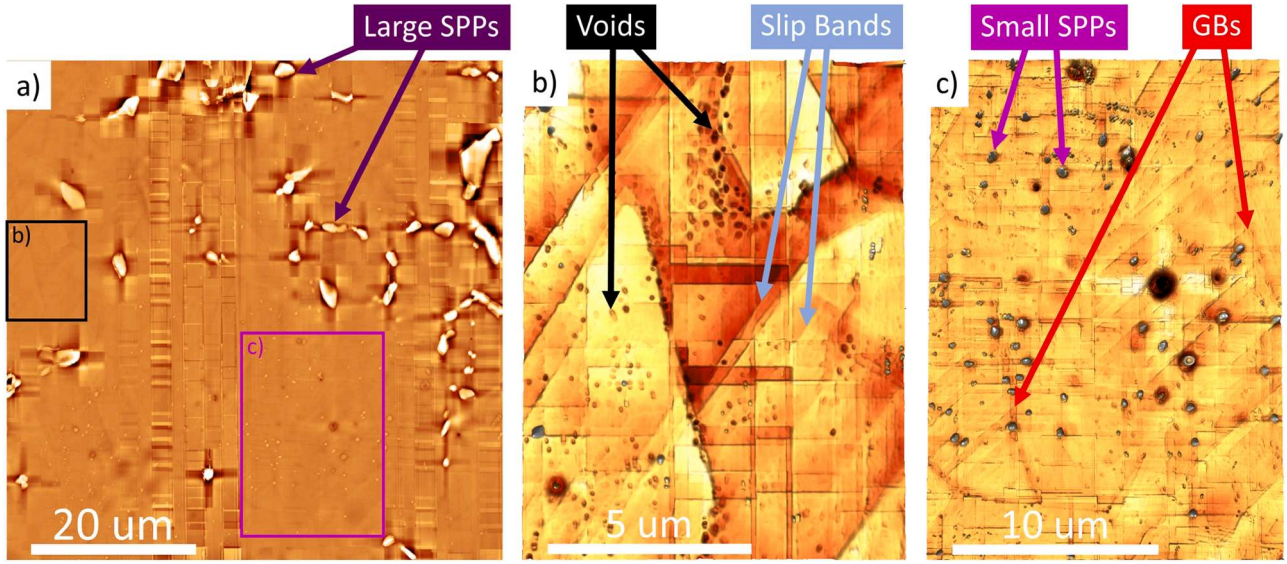

Fig. 2. a) A large area composite HS-AFM topographic map with two smaller composite maps from the regionsoutlined in blue, where: b) highlights a region of a concentration of voids, and c) highlights a region of smaller SPPs. Examples of key microstructural features including SPPs, voids, slip bands and grain boundaries (GBs) are labelled.

are present across the surface indicating that the sample has been plastically stressed. This is likely the result of unintentional bending of the sample during preparation or handling. Fig. 2b and 2c show two smaller composite HS-AFM images, from the regions outlined within the larger composite topographic map. Fig. 2b shows a region containing numerous grain boundaries and a region of a concentration of voids formed due to irradiation. The voids vary in depth, with more frequent and deeper voids appearing to concentrate at the grain boundaries. Fig. 2c shows a region containing a number of smaller SPPs, primarily intragranular.

Correlated EBSD and EDX measurements were performed from a region on the sample surface containing the area analysed by HS-AFM. For direct comparison between maps collected from each technique, Fig. 3 contains rotated and cropped versions of the EBSD and EDX maps such that they coincide with the composite HS-AFM topographic map shown in Fig. 2a.

Inverse pole figure (IPF), phase, and misorientation maps collected by EBSD analysis (Fig. 3c–e, respectively) confirm the intergranular nature of the larger SPPs. Phase information collected in this region was mapped to 3 phases that were expected to be present within the material: face-centred cubic (FCC), sigma phase, and body-centred cubic (BCC). The sample bulk was mapped to FCC (austenite). The majority of large SPPs were identified as FCC, others were identified as BCC or sigma phase. However, measurements performed on SPPs were at a much lower confidence index due to their small size and non-flat surface. Furthermore, the high aspect ratio of the SPPs resulted in a shadowing effect observed as a white (non-indexed) edge in Fig. 3d. In the grain boundary misorientation map (Fig. 3e) each grain boundary was classified as either low-angle grain boundaries (LAGBs), high-angle grain boundaries (HAGBs), or twin boundaries. Grain boundaries with misorientation values $< 5^{\circ}$ are considered to be sub-GBs (i.e. within a grain). Other types of coincident-site lattice (CSL) grain boundaries were not considered within this work. A high proportion of twin boundaries are observed.

EDX analysis (Fig. 3f) shows that the SPPs contain differing ratios of elements, with some appearing to have a compositionally different shell, or altered bulk composition immediately adjacent to where they have formed. Fig. 4 shows the element specific EDX maps for the same region, such that each element may be considered separately. SPPs are considered in more detail in the following section.

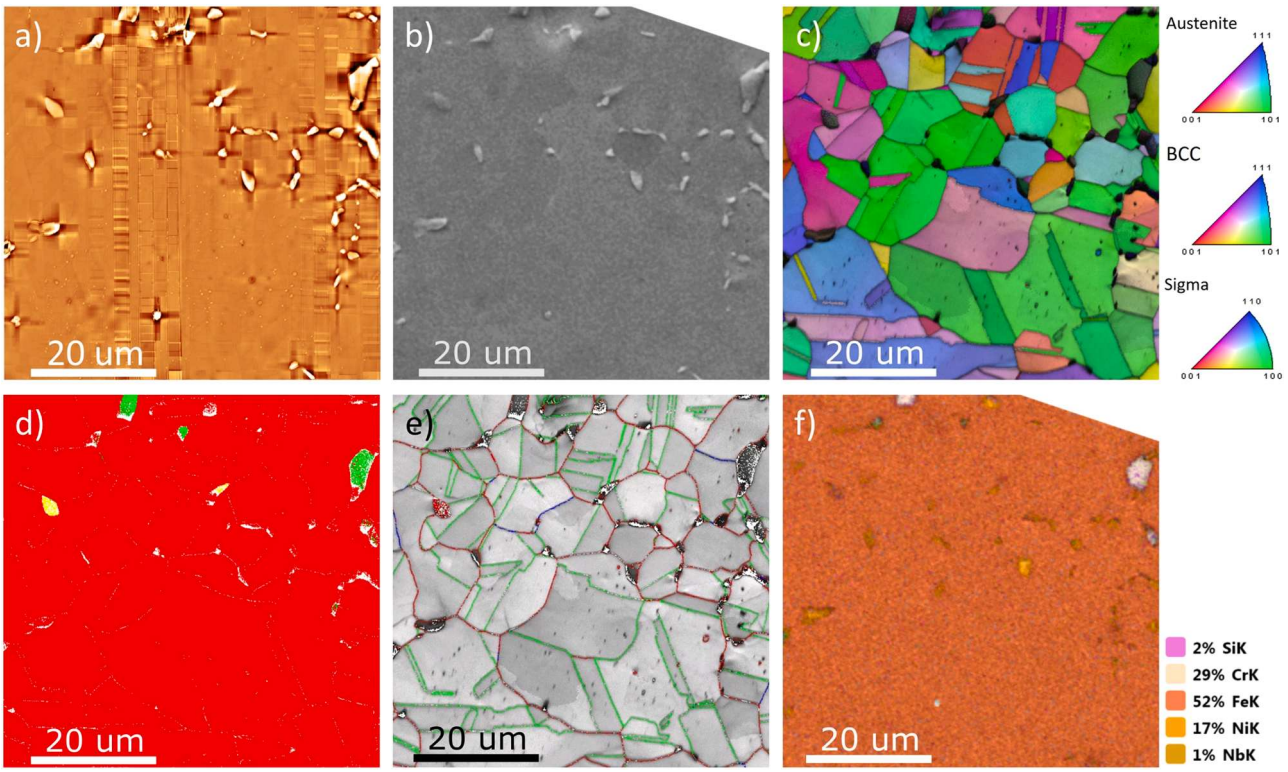

Fig. 3. Large area maps collected from the sample surface rotated and cropped to coincide with the area analysed by HS-AFM: a) HS-AFM topographic map, b) SE image, c) IPF IQ map with inset legend, d) phase map (where red is face-centred cubic (FCC), green is body-centred cubic (BCC), and yellow is sigma phase), e) grain boundary misorientation map (grain boundary misorientation values in the range 5°−15° are indicated in blue, 15°−62.8° in red, and 60° with misorientation axis ⟨ 111 ⟩ in green), and f) EDX elemental composition map with inset legend (individual element maps are given in Fig. 4).

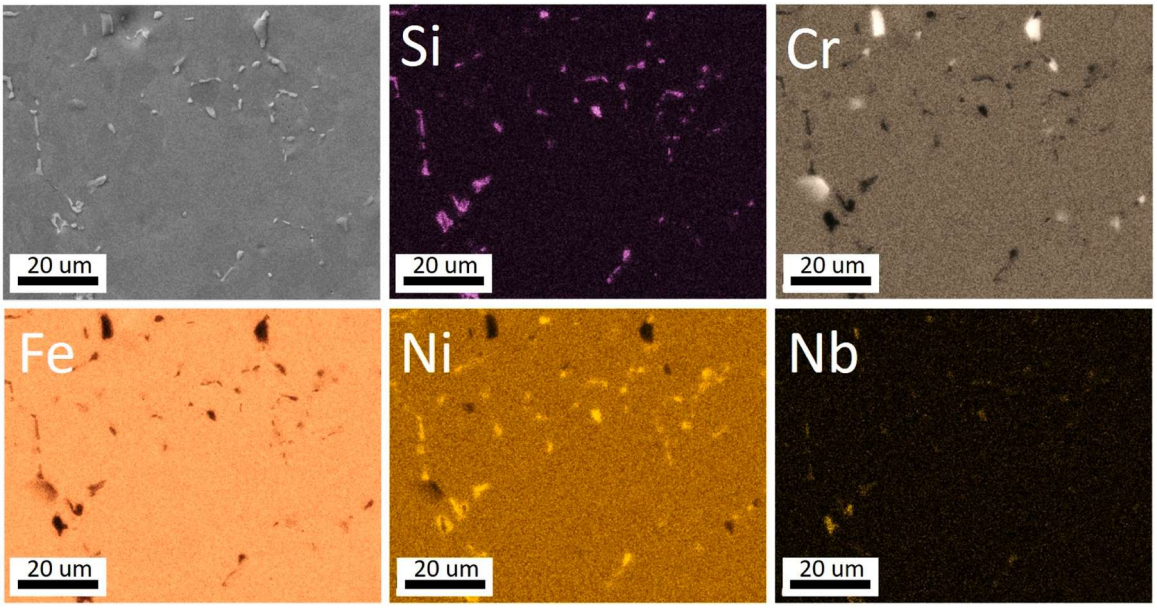

Fig. 4. The first image shows an SE image of the area analysed, the following images show element specific EDX maps collected from the sample surface, where brighter areas contain a higher concentration of the given element, and dark areas contain a lower concentration. Individual element maps are overlayed in Fig. 3f.

3.2. Secondary phase precipitates (SPPs)

3.2.1. Identification of SPPs

Whilst EDX analysis is not of sufficient resolution to allow for accurate identification of SPPs, it may instead be used as an indication of chemical composition and distributions allowing for sufficient confidence when identifying SPPs known to be present. The SPPs expected to be present within the material analysed ($M_{23}C_6$, sigma phase, NbC and G phase) are compositionally distinct and so may be tentatively identified using the EDX maps shown in Figs. 3 and 4. Additional EDX spot analysis was performed at the positions shown in Fig. 5 and the measured elemental compositions are given in Table 2.

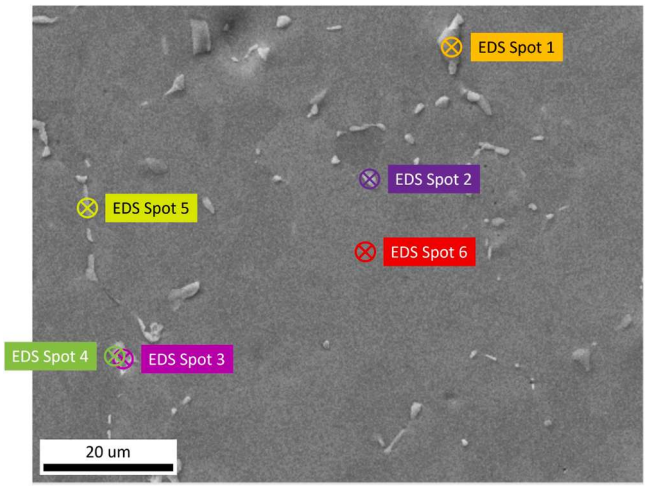

Fig. 5. A reference map showing the locations of EDX spot analysis on the sample surface, measured compositions are given in Table 2.

Table 2
A table of weight% as measured by spot EDX for the positions shown in Fig. 5.

	Si	Cr	Fe	Ni	Nb	Identification
Spot 1	0.02	70.95	20.21	8.04	0.77	M23C6
Spot 2	9.79	8.20	21.45	40.32	20.24	NbC with G Phase Shell
Spot 3	3.55	5.31	12.07	26.30	52.77	NbC
Spot 4	8.13	7.80	20.17	34.58	29.32	G Phase shell
Spot 5	4.99	15.67	42.22	28.84	8.29	G Phase
Spot 6	0.39	20.35	55.92	22.77	0.56	Bulk

$M_{23}C_6$, sigma phase, NbC and G phase were all identified within the sample analysed. SPPs identified as $M_{23}C_6$ carbides were typically larger (up to 4 μm), angular in shape, and intergranular. Spot EDX collected at an $M_{23}C_6$ carbide is labelled as Spot 1 in Fig. 5, additionally an EDX line scan collected across one of these SPPs is shown in Fig. 6a and b. Moving from the bulk to SPP, chromium concentration is observed to increase considerably, iron and nickel are seen to decrease in concentration, and niobium and silicon are unchanged.

Sigma phase was identified initially within the EBSD phase map (Fig. 3d). By comparing this map to the EDX maps (Fig. 4), it can be seen that these SPPs have a high concentration of chromium and an iron concentration comparable to the bulk material, consistent with sigma phase.

The majority of SPPs within the region analysed were identified as NbC and G phase. G phase is known to be primarily composed of nickel, niobium, and silicon, and can therefore be observed within the EDX maps as regions in which these elements are coincident. However, identification of NbC is often complicated by the occurrence of a G phase shell. This phenomenon is demonstrated in Fig. 6c and 6d in which an EDX line scan was collected across an NbC with a G phase shell. The G phase shell was enriched in nickel, silicon, and niobium, and depleted in iron and chromium, with respect to bulk measurements. The NbC core was found to contain an increased concentration of niobium as expected, as well as silicon to some extent, and was depleted in iron and chromium, again, with respect to bulk measurements. Increased silicon is likely due to an overlap in the measurements of NbC and the surrounding G phase shell. Through analysis of the EDX maps combined with EDX spot measurements (Spots 2 and 3 in Fig. 5), it was tentatively concluded that the majority of larger NbC precipitates were observed to have a G phase shell. However, a number of smaller SPPs can be observed in the niobium EDX map which are expected to be NbC prior to the formation of a G phase shell.

3.2.2. *HS-AFM analysis of SPPs*

Following identification of the SPPs in the analysed sample surface area, HS-AFM measurements of each type of SPP were compared in order to ascertain whether HS-AFM topographic analysis would be sufficient for SPP identification under the conditions explored. Fig. 7 shows examples of topographic maps containing SPPs identified as $M_{23}C_6$, sigma phase, G phase, and NbC (with a G phase shell). This figure also shows a selection of topographic maps containing various SPPs that have been cropped such that only the surface textures are within the frame, additional detail was attained by altering the z-scale start and end values.

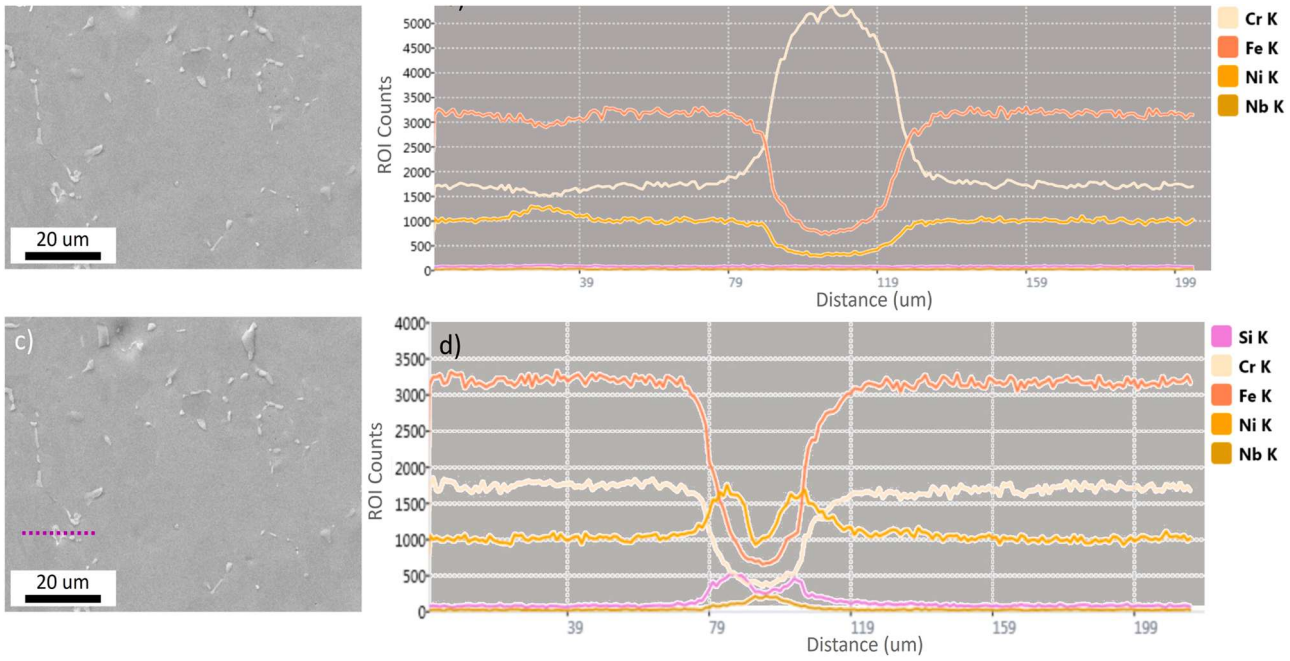

Fig. 6. a) A secondary electron image showing a $M_{23}C_6$ carbide indicated in orange, b) an EDX line scan collected across the orange line, c) a secondary electron image showing an NbC with a G phase shell indicated in purple, and d) an EDX line scan collected across the purple line.

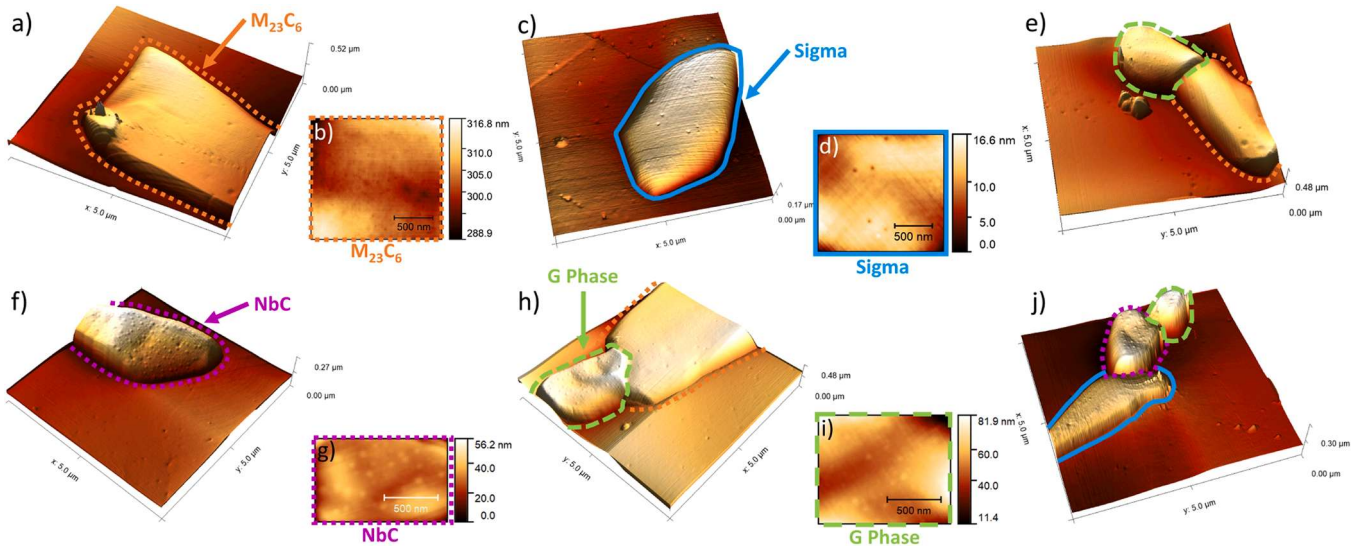

Fig. 7. Images showing HS-AFM 3D topographic maps of regions on the sample surface containing SPPs where a dotted orange line denotes an $M_{23}C_6$ (seen in a, e and h), a solid blue line denotes sigma phase (seen in c and j), a dotted purple line denotes NbC with a G phase shell (seen in f and j), and a dashed green line denotes G phase (seen in e, h, and j). Also shown are cropped topographic maps of the textures observed on the surface of various SPPs: b) $M_{23}C_6$ carbide, d) sigma phase, g) NbC (with a G phase shell), and i) G phase.

When comparing $M_{23}C_6$ carbides and sigma phase a difference in height is observed as well as differences in surface texture (Fig. 7). $M_{23}C_6$ carbides are observed to be around 250 nm in height, with a sharp step height at the edge of the SPP. Sigma phase on the other hand was around 120 nm in height and observed to have smooth edge step to the bulk. Fig. 7b and d show that both $M_{23}C_6$ and sigma phase have patterns of negative features on their surface. Generally, the features present on $M_{23}C_6$ are much smaller and more frequent than those observed on sigma phase. The negative features observed on the sigma phase are similar to the voids observed across the bulk of the sample.

A comparison between G phase and NbC with a G phase shell reveals little topographic difference (Fig. 7). Both SPPs are of comparable shape and topographic height, with similar surface textures. The surface textures on NbC (with a G phase shell) and G phase are shown in Fig. 7g and i, respectively. Both SPPs have a dotted pattern of positive features on their surface.

A number of smaller SPPs were also observed by HS-AFM, some of these SPPs are shown in Fig. 8. By comparing the HS-AFM maps and the EDX niobium map (Fig. 4), these features may be identified as NbC SPPs. In contrast with larger NbC precipitates, these smaller NbC were intragranular, circular, and bowed in the centre.

3.3. Voids

3.3.1. Large area statistical analysis of void distribution

From initial observations of the surface by HS-AFM, voids were observed to concentrate along or near certain grain boundaries. Analysis of the distribution of voids present across the surface was performed using bespoke software (Nanomapper - Bristol Nano Dynamics Ltd. UK). The data used for this analysis is the same data collected for the large area composite HS-AFM map shown in Fig. 2a. As a result, analysed frames will overlap with one another, and features will be counted more than once, these data should therefore be considered as indicative of the patterns and relative frequencies of void size and distribution.

Within this analysis, a feature was identified as a void if it was a negative feature (in the z-direction) with a bounding rectangle width of 1–500 nm and length of 1–500 nm, and a ratio of ellipse axes between 0.5 and 3. HS-AFM data used within this analysis was first processed to allow for clearer images of voids, this is particularly important for regions surrounding high features such as large SPPs. The data was processed through a frequency filter and a relative standard deviation of 2.5 was applied. This resulted in the thresholding of negative features with depth greater than 2.5 relative standard deviation, in order to differentiate between voids and other surface height changes. This data was used to plot a histogram of the void size, shown in Fig. 9a. The voids were found to have a mean void diameter of 75 nm, with a mode of 66 nm. The distribution was found to follow a long-tailed distribution and so a log-normal fit was performed in Origin software, shown in red in Fig. 9a. The log-normal fit had a peak at 64 nm. A heat map of features identified as voids is shown in Fig. 9b. This map indicates an inhomogeneous distribution of voids, with regions of high and low concentrations of voids.

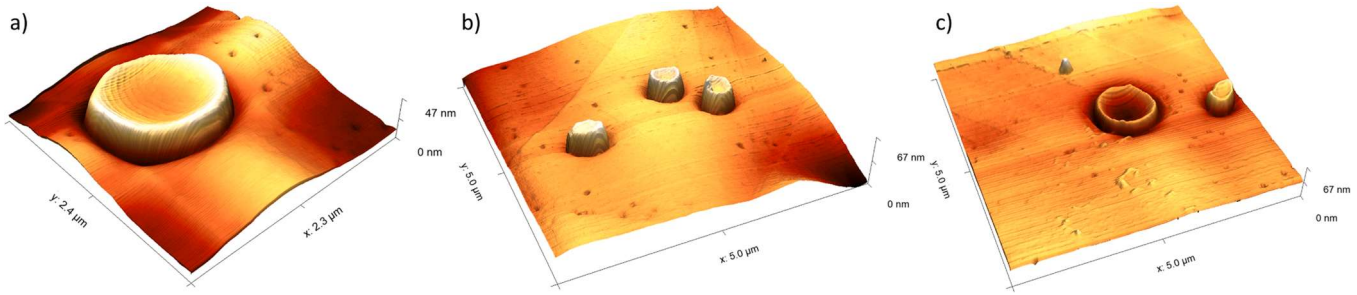

Fig. 8. a)-c) 3D HS-AFM topographic maps of smaller SPPs identified at NbC on the sample surface.

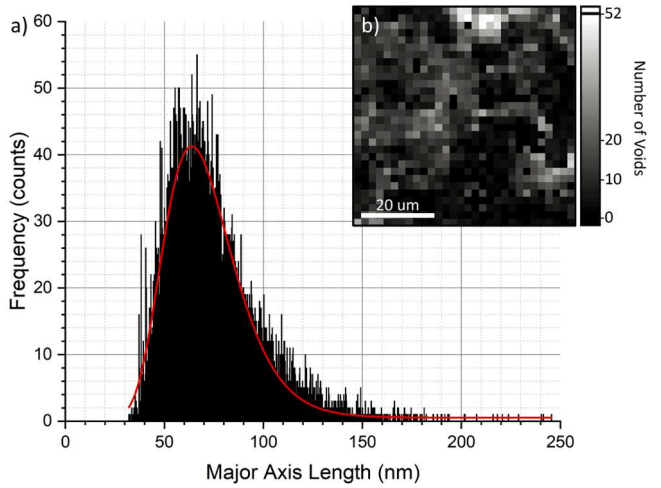

Fig. 9. a)A histogram showing the major axis length of the voids measured by HS-AFM, with a log-normal fit shown in red. Inset b) shows a heat map for the region on the sample surface analysed by HS-AFM, where lighter areas have a higher number density of features identified as voids, and darker areas have a lower number density.

3.3.2. *Analysis of individual HS-AFM frames*

HS-AFM data was analysed frame by frame to build up a database of images containing HAGBs, LAGBs, and twin boundaries, as identified by EBSD (Fig. 3e). Example topographic maps are given in Fig. 10a, d, g, and j. It can be seen that HAGBs are clearest within HS-AFM topographic maps, with LAGBs appearing much less prominently. This is in part due to HAGBs appearing darker (i.e. lower topographically) but also due to the presence of dislocations across the surface, as the dislocation direction varies from grain to grain either side of HAGBs. In contrast, dislocations are able to move through LAGBs, making them more difficult to observe topographically, as observed in Fig. 10d and j.

Fig. 10 show that voids concentrate along grain boundaries. Topographic line scans were performed across more than 100 individual voids, these measurements are summarised in Table 3. Voids were found to be more densely distributed, deeper, and have a larger diameter at

Table 3
Measured void diameters and depths for different regions on the surface (bulk and grain boundaries), and different grain boundary types. Averages were calculated from 85 line scans across voids in the bulk, 73 line scans across voids on HAGBs, 14 on LAGBs, and 15 twin boundaries.

Region Type	Void Diameter (nm)		Void Depth (nm)		No. of Voids Measured
	Mean	Range	Mean	Range	
Grain Boundary	134	60 - 270	6.1	0.9 - 20	102
Bulk	100	50 - 200	2.2	0.4 - 8	85
Grain Boundary Type	**Void Diameter (nm) Mean**	**Range**	**Void Depth (nm) Mean**	**Range**	**No. of Voids Measured**
HAGB	143	70 - 270	7.2	1 - 20	73
LAGB	108	65 - 200	2.9	0.9 - 10	14
Twin	113	60 - 180	3.4	0.9 - 9.5	15

HAGBs when compared to LAGBs or twin boundaries. Fig. 10j contains a concentration of voids that appear to bridge from one HAGB to another. By comparing the known location at which this map was collected with the EBSD maps collected from the region, these two grain boundaries are either side of a thin cross section of a grain.

Voids measured along twin boundaries were varied, but were typically smaller in diameter than for HAGBs, and less frequent, as observed in Fig. 10a, g, and j. Fig. 10a contains a twin boundary with non-coherent twin steps. In this case, voids were located in such a way that they appeared to pin the grain boundary at the turning point. Fig. 10d and j contain LAGBs. Again, voids were observed to line-up along these grain boundaries, these voids were often shallow. Voids were also aligned along slip dislocations; in turn these voids must also align along crystallographic planes in the material. Some voids, however, do not appear to follow any clear pattern.

4. Discussion

Measurements performed on a sample of ex-service AGR cladding focussed on analysis of surface microstructures by HS-AFM and other correlative techniques including EBSD and EDX. Analysis by HS-AFM has not been performed on ex-service AGR cladding prior to this work

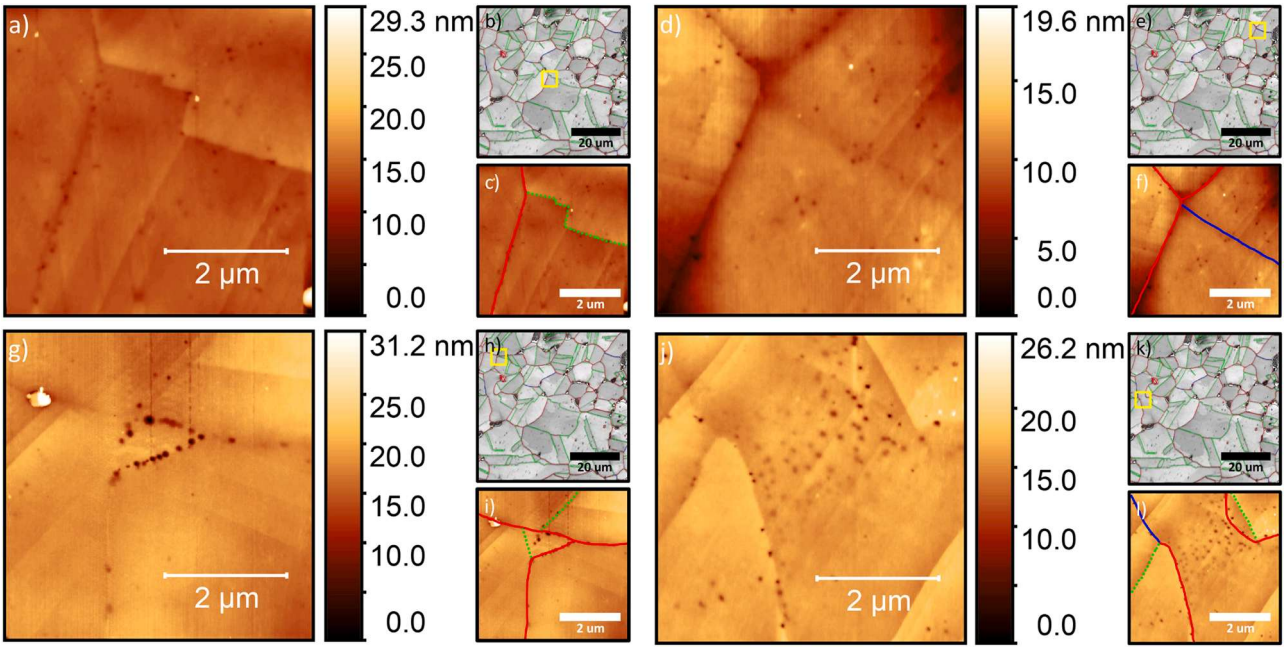

Fig. 10. a, d, g, and j) A series of HS-AFM topographic maps showing grain boundaries with, b, e, h, and k) EBSD misorientation maps with HS-AFM map location outlined in yellow, and c, f, i, and l) copies of HS-AFM maps with labelled HAGBs (in red), LAGBs (in blue), and twin boundaries (dotted in green).

and so offers an opportunity for novel characterisation. Large area analysis by HS-AFM and SEM techniques revealed widespread precipitation in the region analysed. Due to the large height of the SPPs across the surface HS-AFM images collected in the vicinity of SPPs exhibited imaging artefacts. This also affected EBSD images, where shadowing was observed. It is expected that this effect would be reduced if the samples were mechanically polished. HS-AFM analysis also revealed numerous voids across the surface. These features are discussed in greater detail in the following sections. Analysis of the microstructure by EBSD found the grain size (diameter) varied from approximately 0.1 μm to 30.8 μm, with an average diameter of 1.4 μm and a standard deviation of 3.9 μm.

4.1. Secondary phase precipitates

Numerous SPPs with varying morphologies were observed across the sample surface during large area mapping (Figs. 1–4). Larger SPPs were primarily intergranular, including some appearing on twin boundaries. These SPPs were identified by cross analysing the large area maps (Fig. 3), performing additional spot EDX analysis, and comparing to literature. The larger SPPs were identified as $M_{23}C_6$, sigma phase, NbC (with G phase shell), and G phase. HS-AFM analysis revealed numerous smaller SPPs present across the sample, identified as NbC. These SPPs, with the exception of NbC, are known to form as a result of prolonged in-service conditions and are not present in non-irradiated 20Cr/25Ni-Nb (see Supplementary Information for additional analysis collected from a non-irradiated specimen of AGR cladding material) [6,17,18].

The majority of the larger SPPs were identified as G phase, as evident from the silicon and nickel EDX maps in Fig. 4. G phase is not expected to have a significant effect on the corrosion susceptibility of the material, however nickel-rich SPPs such as G phase may result in local instabilities of the austenite [17]. G phase can also lead to hardening, which in turn affects mechanical aspects of SCC susceptibility and behaviour. NbC observed within the analysed sample varied in shape and size. Smaller NbC observed by HS-AFM were primarily intragranular, circular in cross section and up to 1 μm in diameter. Large NbC was intergranular and irregular in shape, with some appearing globular, plate-like, or sometimes elongated. Niobium is added to 20Cr/25Ni-Nb as a stabiliser to deter chromium-rich carbide precipitate formation by preferentially forming NbC. The presence of NbC is therefore considered as beneficial for the corrosion properties of the material. However, recent works have found that NbC may act as initiation sites for localised corrosion processes such as pitting, as they are cathodically active leading to adjacent anodic dissolution [6]. Larger NbC precipitates were found to contain a shell of a phase identified as G phase. This suggests that G phase formation had nucleated on the NbC precipitate, and that this evolution had initiated at the outer layers. This phenomenon has been reported in previous works using proton irradiated samples [1].

A number of chromium-rich phases were identified as $M_{23}C_6$ and sigma phase. $M_{23}C_6$ observed within the sample were located along grain boundaries, with the largest precipitates appearing on the same scale as grains (Fig. 3). $M_{23}C_6$ precipitates varied in shape, with some appearing plate-like and others appearing more globular. $M_{23}C_6$ precipitates are known to form readily within austenitic stainless steels. These precipitates were often associated with G phase, as is expected from previous studies [17]. This is thought to be due to a local enhancement of carbon (and nitrogen) following the formation of G phase from NbC, discussed previously [17]. The presence of chromium-rich precipitates, such as $M_{23}C_6$, may adversely influence corrosion behaviour and lower resistance to IGSCC [28,29]. $M_{23}C_6$ formation has also been associated with loss of ductility and toughness [28].

Large sigma phase precipitates appeared plate-like in shape. Sigma phase is known to primarily form along grain boundaries but can be found within the grain for samples at longer ageing times [17,28]. Sigma phase is known to form preferentially at ferritic regions [30,31]. Sigma phase formation is therefore promoted by the formation of G phase through destabilising the austenite, hence an association exists between the two phases, as observed within this work [17]. The presence of sigma phase can result in embrittlement of the metal [30,31]. Whilst this would be an issue for primary structural components, this is generally less impactful for fuel cladding due to the lower associated stress requirements. However, sigma phase precipitation can also result in chromium-depleted regions in the adjacent matrix, leading to local corrosion susceptibility and associated risk of cracking at much lower stress levels [28,30,31].

4.1.1. HS-AFM analysis of SPPs

HS-AFM analysis of SPPs found that the heights and surface topographies varied with each type of SPP. $M_{23}C_6$ and sigma phase contained varying patterns of negative features across their surface, with differences in size and number density. Both of these SPPs are chromium-rich, and so may result in similar responses to the electrolytic etch. The negative features observed on the sigma phase were similar to the voids observed in the sample bulk, indicating that such features may have formed in service rather than as a result of sample preparation.

The negative features present on both $M_{23}C_6$ and sigma phase contrast the positive features present on NbC and G phase. The dotted texture of positive features may be the result of atomic clustering on the surface of the SPP. The similar appearance in NbC and G phase is likely the result of a G phase shell surrounding the NbC, as identified by EDX measurements. This is not expected to be the case if the sample were mechanically polished to produce a genuine cross section, however this surface was electrolytically etched and will differ as a result [32]. Positive features present on NbC with a G phase shell is more densely patterned than that observed on the surface of G phase. This may give insight into the method of formation and growth as the G phase shell evolves.

From this analysis it is envisioned that measurements collected by HS-AFM may give an indication of the SPPs present, by topography and surface texture. These topographies and textures are affected by surface preparation methods, the resultant surface will be a convolution of the surface microstructure and their respective responses to the etch conditions. Resultant topographies are expected to also be affected by thermal history and irradiation conditions. As an extension to this work, different etch conditions and sample preparation methods could be explored.

4.2. Voids

HS-AFM analysis revealed numerous features across the surface which may be identified as plastic voids, helium bubbles, or cavities [10]. These features are referred to as voids. These voids were circular in cross section and varied in size and depth. In previous studies these features have only been observed in transmission electron microscopy (TEM) analysis. Irradiation can result in the void formation through the production of helium from neutron induced transmutation of nickel and subsequent decay chain [33]. Helium then stabilises vacancy clusters, forming void cavities [11,33]. These voids are not present in non-irradiated 20Cr/25Ni-Nb and therefore are attributed to the thermal and irradiation conditions in-reactor (see Supplementary Information).

Voids were found to concentrate along the grain boundaries where they were wider (mean diameter 34 nm larger) and deeper (mean depth 3.9 nm larger), in some cases coalescing to form concentrated clusters (Fig. 2b). This may be explained as the grain boundary acts as a defect sink and so voids formed as crystal defects (i.e. vacancies) may migrate towards grain boundaries [1,10,11]. Differences in size and depth were observed when comparing HAGBs, LAGBs, and twin boundaries (Fig. 10 and summarised in Table 3). Larger and deeper voids were often located along HAGBs. In some cases, the severity of this effect was such that the grain boundary appeared almost perforated. In Fig. 10j numerous voids

were observed between two HAGBs. This was found to be the result of a thin grain cross section at the surface. This is a rare insight into how the voids are distributed throughout a grain boundary in 3D. In comparison, voids observed along coherent twin boundaries or LAGBs were smaller and shallower, likely due to these grain boundary types acting as less efficient sinks [1,8,34]. Voids were also observed to align along slip dislocations, therefore following the crystallographic planes in the material. Nevertheless, some voids did not appear to follow any clear or obvious pattern.

By comparing the heat map (Fig. 9b) to the large area analysis shown in Fig. 3, a possible association with SPPs is observed. Such features are known to act as alternative defect sinks [1]. Generally, areas of high numbers of voids also aligned well with HAGBs. An area sparse in voids is seen in the bottom right hand quarter. This area aligned well with a region of twin boundaries and a lack of large SPPs.

The formation of inter- and intragranular voids can lead to adverse phenomena, such as embrittlement [10,11]. Large agglomerations of bubbles/voids may also result in swelling and local stresses [16]. As larger voids were located along grain boundaries, this may have an adverse effect on IGSCC susceptibility [11,16]. The results described in this work demonstrate the applicability of HS-AFM in the study of the effects of combined high-temperature and neutron irradiation conditions experienced in-reactor. The analysis performed offers new insight in the distribution of void size and frequency in relation to other microstructural features such as SPPs, LAGBs, HAGBs and twin boundaries, in an ex-service specimen.

5. Conclusions

A study of irradiated microstructure in a sample of ex-service irradiated AGR fuel cladding was performed using a variety of complementary techniques. Large area analysis of ex-service AGR fuel cladding by HS-AFM, EBSD, and EDX provided correlated topographic, crystallographic, and chemical information from the sample surface. This allowed for identification of SPPs and analysis of irradiated microstructure. Further HS-AFM analysis of SPPs and voids was performed to assess the information attainable through topographic analysis for the first time.

The analysis performed in this study offers new insights into the microstructural changes effecting AGR cladding material following the high temperature neutron irradiation conditions experienced in-reactor. The following conclusions are drawn from this work:

- Large area analysis of a sample of ex-service AGR fuel cladding revealed numerous large SPPs including: $M_{23}C_6$, sigma phase, NbC, and G phase. These precipitates were primarily intergranular. Numerous smaller NbC were found to be primarily intragranular.
- HS-AFM analysis of SPPs revealed surface textures unique to each SPP type, with the exception of NbC due to the presence of a G phase shell. This study introduced the potential of SPP identification by HSAFM due to chemically induced topography. This may be extended to alternative electrolytic etch recipes for comparative studies with the potential to probe the chemical behaviours of the surface microstructural features by performing numerous subsequent etches.
- Numerous nm-scale voids were observed across the surface by HS-AFM, with intergranular voids appearing larger in size and depth. These voids had previously only been observed by TEM. The high throughput of HS-AFM allowed for large area analysis providing various surface statistics such as void size and variation. Voids were found to be larger and deeper at grain boundaries, particularly HAGBs. An association was also noted between increased void frequency and SPPs.

CRediT authorship contribution statement

S. Moore: Conceptualization, Data curation, Formal analysis, Investigation, Methodology, Writing – original draft, Writing – review & editing. **R. Burrows:** Conceptualization, Formal analysis, Funding acquisition, Investigation, Methodology, Resources, Supervision, Writing – review & editing. **A.D. Warren:** Formal analysis, Investigation, Methodology, Writing – review & editing. **D. Hambley:** Conceptualization, Formal analysis, Funding acquisition, Resources, Writing – review & editing. **F.S. Russell-Pavier:** Data curation, Formal analysis, Software, Writing – review & editing. **T.L. Martin:** Formal analysis, Supervision, Writing – review & editing. **L. Picco:** Conceptualization, Formal analysis, Funding acquisition, Methodology, Resources, Software, Supervision, Writing – review & editing. **O.D. Payton:** Conceptualization, Funding acquisition, Investigation, Methodology, Resources, Software, Supervision, Writing – review & editing.

Declaration of competing interest

Oliver Payton and Loren Picco are shareholders in Bristol Nano Dynamics Ltd., a University of Bristol spin-out company which manufacture the HS-AFM instrumentation used within this work. Other authors have no competing interests to declare.

Data availability

Data will be made available on request.

Acknowledgements

The authors would like to thank the physics workshop at the University of Bristol. The PhD studentship for S.M. was funded by the National Nuclear Laboratory (NNL) and the Engineering and Physical Sciences Research Council (EPSRC). This research did not receive any specific grant from funding agencies in the public, commercial, or not-for-profit sectors.

Supplementary materials

Supplementary material associated with this article can be found, in the online version, at doi:10.1016/j.jnucmat.2024.155265.

References

[1] C. Barcellini, R. Harrison, S. Dumbill, S. Donnelly, E. Jimenez-Melero, Local chemical instabilities in 20Cr25Ni Nb-stabilised austenitic stainless steel induced by proton irradiation, J. Nucl. Mater. 518 (2019) 95–107.
[2] E. Howett, C. Boxall, D. Hambley, AGR cladding corrosion: investigation of the effect of temperature on unsensitized stainless steel, MRS Adv. 2 (11) (2017) 615–620.
[3] C. Anwyl, C. Boxall, R. Wilbraham, D. Hambley, C. Padovani, Corrosion of AGR fuel pin steel under conditions relevant to permanent disposal, Procedia Chem. 21 (2016) 247–254.
[4] A. Al-Shater, D. Engelberg, S. Lyon, C. Donohoe, S. Walters, G. Whillock, A. Sherry, Characterization of the stress corrosion cracking behavior of thermally sensitized 20Cr-25Ni stainless steel in a simulated cooling pond environment, J. Nucl. Sci. Technol. 54 (7) (2017) 742–751.
[5] J.B. Goode, D. Harbottle, B.C. Hanson, Vacuum drying of advanced gas reactor fuel, Progr. Nucl. Energy 109 (2018) 145–158.
[6] R.N. Clark, J. Searle, T.L. Martin, W. Walters, G. Williams, The role of niobium carbides in the localised corrosion initiation of 20Cr-25Ni-Nb advanced gas-cooled reactor fuel cladding, Corros. Sci. 165 (2020) 108365.
[7] G.O. Whillock, B.J. Hands, T.P. Majchrowski, D.I. Hambley, Investigation of thermally sensitised stainless steels as analogues for spent AGR fuel cladding to test a corrosion inhibitor for intergranular stress corrosion cracking, J. Nucl. Mater. 498 (2018) 187–198.
[8] C.M. Barr, L. Barnard, J.E. Nathaniel, K. Hattar, K.A. Unocic, I. Szlurfarska, D. Morgan, M.L. Taheri, Grain boundary character dependence of radiation-induced segregation in a model Ni-Cr alloy, J. Mater. Res. 30 (9) (2015) 1290.
[9] G.S. Was, S.M. Bruemmer, Effects of irradiation on intergranular stress corrosion cracking, J. Nucl. Mater. 216 (1994) 326–347.

[10] O. Chopra, A. Rao, A review of irradiation effects on LWR core internal materials–IASCC susceptibility and crack growth rates of austenitic stainless steels, J. Nucl. Mater. 409 (3) (2011) 235–256.
[11] P. Scott, A review of irradiation assisted stress corrosion cracking, J. Nucl. Mater. 211 (2) (1994) 101–122.
[12] S.M. Bruemmer, E.P. Simonen, P.M. Scott, P.L. Andresen, G.S. Was, J.L. Nelson, Radiation-induced material changes and susceptibility to intergranular failure of light-water-reactor core internals, J. Nucl. Mater. 274 (3) (1999) 299–314.
[13] Z. Lu, R. Faulkner, G. Was, B. Wirth, Irradiation-induced grain boundary chromium microchemistry in high alloy ferritic steels, Scr. Mater. 58 (10) (2008) 878–881.
[14] P.E.J. Flewitt and R.K. Wild, *Grain boundaries: their microstructure and chemistry*. 2001.
[15] E. Lee, P. Maziasz, A. Rowcliffe, Structure and composition of phases occurring in austenitic stainless steels in thermal and irradiation environments, tech. rep (1980).
[16] S.J. Zinkle, G. Was, Materials challenges in nuclear energy, Acta Mater. 61 (3) (2013) 735–758.
[17] D. Powell, R. Pilkington, D. Miller, The precipitation characteristics of 20% Cr/25% Ni-Nb stabilised stainless steel, Acta Metallurg. 36 (3) (1988) 713–724.
[18] T. Sourmail, Precipitation in creep resistant austenitic stainless steels, Mater. Sci. Technol. 17 (1) (2001) 1–14.
[19] O. Payton, L. Picco, T. Scott, High-speed atomic force microscopy for materials science, Int. Mater. Rev. 61 (8) (2016) 473–494.
[20] R.N. Clark, R. Burrows, R. Patel, S. Moore, K.R. Hallam, P.E. Flewitt, Nanometre to micrometre length-scale techniques for characterising environmentally-assisted cracking: an appraisal, Heliyon 6 (3) (2020) e03448.
[21] A. Laferrere, R. Burrows, C. Glover, R.N. Clark, O. Payton, L. Picco, S. Moore, G. Williams, In situ imaging of corrosion processes in nuclear fuel cladding, Corros. Eng. Sci. Technol. 52 (8) (2017) 596–604.
[22] S. Moore, R. Burrows, L. Picco, T.L. Martin, S.J. Greenwell, T.B. Scott, O.D. Payton, A study of dynamic nanoscale corrosion initiation events using hs-afm, Faraday Discuss. 210 (2018) 409–428.
[23] S. Moore, R. Burrows, D. Kumar, M. Kloucek, A. Warren, P. Flewitt, L. Picco, O. Payton, T. Martin, Observation of stress corrosion cracking using real-time in situ high-speed atomic force microscopy and correlative techniques, npj Mater. Degrad. 5 (1) (2021) 1–10.
[24] S. Moore, R. Burrows, L. Picco, O.D. Payton, T.L. Martin, Real-time and correlative imaging of localised corrosion events by high-speed atomic force microscopy, Microsc. Microanaly. 28 (S1) (2022) 2116–2117.
[25] E. Nonbel, "Description of the advanced gas cooled type of reactor," Risø National Laboratory, NKS/RAK2 (96) TR-C2, 1996.
[26] D. Nečas, P. Klapetek, Gwyddion: an open-source software for SPM data analysis, Open Phys. 10 (1) (2012) 181–188.
[27] F. Russell-Pavier, Hi-Fi Nanoscience. Exploring the Nanoscale with Optical Pickup Units, University of Bristol, 2020, p. 183. PhD thesisChapter 6, Section 6.5.
[28] A. Padilha, P. Rios, Decomposition of austenite in austenitic stainless steels, ISIJ Int. 42 (4) (2002) 325–327.
[29] V. Raja, T. Shoji, Stress Corrosion cracking: Theory and Practice, Elsevier, 2011.
[30] C.-C. Hsieh, W. Wu, Overview of intermetallic sigma phase precipitation in stainless steels, Isrn Metallu. 2012 (2012).
[31] C. Tseng, Y. Shen, S. Thompson, M. Mataya, G. Krauss, Fracture and the formation of sigma phase, M23C6, and austenite from delta-ferrite in an AlSI 304L stainless steel, Metallurg. Mater. Transact. A 25 (6) (1994) 1147–1158.
[32] S. Moore, A.D. Warren, R. Burrows, O.D. Payton, L. Picco, F.S. Russell-Pavier, P. G. Martin, T.L. Martin, Sample preparation methods for optimal hs-afm analysis: duplex stainless steel, Ultramicroscopy 222 (2021) 113210.
[33] C. Barcellini, R. Harrison, S. Dumbill, S. Donnelly, E. Jimenez-Melero, Evolution of radiation-induced lattice defects in 20/25 Nb-stabilised austenitic stainless steel during in-situ proton irradiation, J. Nucl. Mater. 514 (2019) 90–100.
[34] A.H. King, S. Shekhar, What does it mean to be special? the significance and application of the Brandon criterion, J. Mater. Sci. 41 (23) (2006) 7675–7682.